Geophys. J. Int. (2004) **159,** 275–290 doi: 10.1111/j.1365-246X.2004.02381.x

Delay times and shear wave splitting in the Mediterranean region

Christian Schmid, Suzan van der Lee* and Domenico Giardini

ETH Zürich, Institute of Geophysics, ETH Hönggerberg(HPP), 8093 *Zürich, Switzerland. E-mail: cschmid@tomo.ig.erdw.ethz.ch*

Accepted 2004 June 8. Received 2004 May 31; in original form 2003 December 8

SUMMARY

We measure *SKS* splitting parameters and *P* and *S* delay times in the Mediterranean region using broad-band recordings from the temporary MIDSEA array and permanent networks. The MIDSEA seismic array has substantially improved data coverage along the European–Mediterranean margins and in northern Africa. Shear wave splitting is observed for 95 per cent of the stations, with splitting times up to 2 s. We propose five anisotropic domains, based on the characteristics of the observations. In the western part of the region we observe an alignment with plate motion, suggesting an asthenospheric origin for anisotropy. In the central and near eastern part, the fast directions are less coherent laterally and influenced by extension and subduction processes. Along the Dead Sea fault the fast directions are parallel to the relative motion between Arabia and Africa, which we attribute in part to coherent vertical deformation. Our measurements of teleseismic, relative *P*- and *S*-wave delay times within the Mediterranean region reach peak-to-peak values of 2.5 and 8 s, respectively. Consistent with International Seismological Centre (ISC) delay times, we observe the earliest arrivals along the Hellenic subduction zone and some of the latest along the Dead Sea fault. We find that *S*-wave delays are roughly three times as large as those of *P* waves. From a slight frequency dependence of our cross-correlation based delay time measurements, we estimate Mediterranean lateral heterogeneity to have a dominant size of one or more hundred kilometres. We further determine that the anisotropy implied by our *SKS* splitting measurements does not significantly bias the pattern of teleseismic delay times.

Key words: anisotropy, delay times, mantle flow, Mediterranean, MIDSEA, subduction.

1 INTRODUCTION

The plate boundary between Africa and Eurasia is not well defined everywhere and several microplates have been proposed to exist in the Mediterranean region (Fig. 1). Overall, Africa and Eurasia have been converging, which has resulted in the numerous arcuate orogenies characteristic of the Mediterranean region. On smaller spatial scales, strike-slip and extension also govern deformation, such as for the Tyrrhenian and Aegean seas, which formed relatively rapidly through backarc extension.

The highest rate of extension is presently observed in the Aegean sea, which is the backarc basin of subduction of Mesozoic oceanic lithosphere beneath the Hellenic arc. In the past, extension was most rapid in the western part of the Mediterranean region. Around 30 Ma, a trench was located roughly along the present east coast of Spain. Subduction then shifted eastwards and evolved into subduction of the Ionian lithosphere beneath the Calabrian arc in southern Italy. This shift resulted in the formation of the western Mediterranean basins, such as the Tyrrhenian sea.

Seismic evaluations of the elastic properties of the upper mantle and crust below the Eurasia–Africa plate boundary region and its different domains of deformation and relative rigidity have been hampered by an uneven distribution of broad-band seismic stations. The MIDSEA project (Van der Lee *et al.* 2001) was launched in order to improve this station distribution and advance our knowledge of the structure of the Earth in this plate boundary region.

Here, we use the data recorded by the MIDSEA and other seismic stations in the Mediterranean region to investigate lateral variations in isotropic and anisotropic seismic velocity. We do so by studying the arrival time delays of teleseismic body waves recorded by the MIDSEA and other broad-band seismic stations in the Mediterranean region and by analyzing split *SKS* waves.

Split *SKS* waves are diagnostic of azimuthal anisotropy in seismic velocity (Savage 1999). Most minerals are anisotropic, but their random distribution in rocks makes the Earth isotropic for seismic wave propagation. However, under special circumstances anisotropy may develop on larger scales. In the mantle, large-scale deformation may result in anisotropy (Hess 1964) as a result of a preferential alignment of the mantle minerals. Anisotropy in the crust is often explained by a preferred orientation of cracks (Crampin 1981).

Relative delay times of teleseismic body waves are diagnostic of lateral heterogeneity in structure of the Earth beneath the recording seismic array. This heterogeneity is caused by spatial variations in crustal rock properties, crustal thickness, mantle temperature and mantle composition. Lithosphere of one plate that subducts beneath

*Now at: Dept. of Geological Sciences, 1850 Campus Drive, Northwestern University, Evanston, IL 60208-2150, USA.

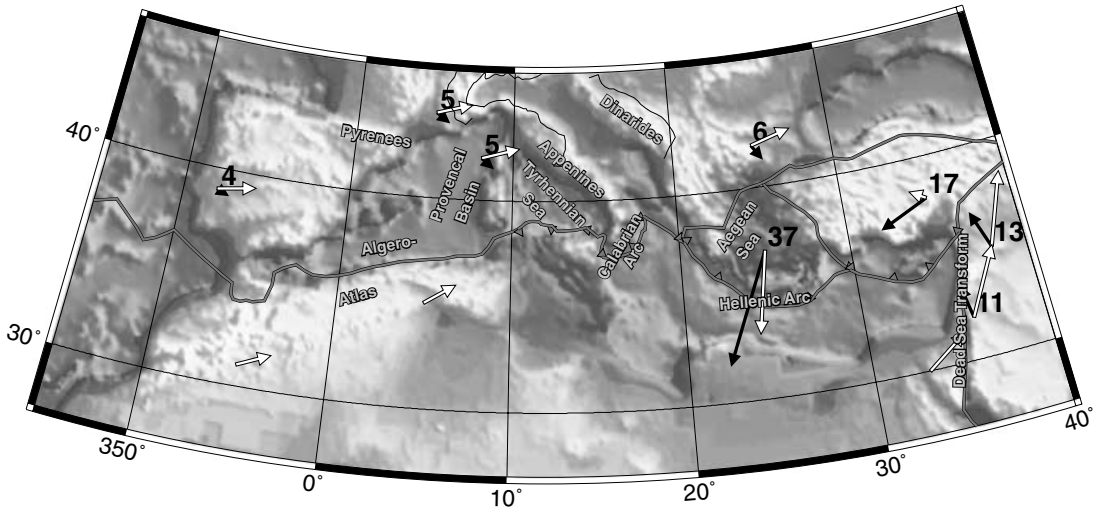

Figure 1. Tectonic map of the Mediterranean region, with topography. Included are simplified plate boundaries (black lines) and plate velocities (black and white arrows), taken from the global plate boundary model PB2002 of Bird (2003; in reality the boundary is much more complex). Black arrows are proportional to plate velocities relative to a fixed Africa, while the white include the motion of Africa relative to the hotspots (Müller *et al.* 1993).

another will constitute a relatively cold zone in the mantle, which causes arrival time delays to be negative. We find positive delays beneath extending basins.

However, anisotropy can also contribute to body wave traveltime delays. In seismic tomography, the delay times are attributed completely to isotropic heterogeneity. On the other hand, delay patterns are also interpreted as caused completely by anisotropy (Babuška *et al.* 1993). Here, we test the potential of our observed delay time pattern to determine azimuthal anisotropy by comparing the azimuthal dependence of observed *P*-wave delay times to the measured polarization directions of the fast part of split *SKS* waves. We also assess the relative contributions of azimuthal anisotropy and lateral heterogeneity to the observed delay times by comparing the observed delay times with those predicted by the pattern of anisotropy derived from observed *SKS* splitting.

2 SHEAR WAVE SPLITTING ANALYSIS

A shear wave passing through an anisotropic medium is split into two orthogonal *S* waves travelling with different velocities and arriving at the receiver at different times. This time difference is proportional to the strength of anisotropy and length of the path in the anisotropic medium. Most splitting studies are of *SKS*, but in principle every shear arrival could be used. The benefit of using *SKS* is that owing to its passage through the liquid outer core of the Earth as a compressional wave, it is radially polarized and only contains an anisotropic signal from the receiver side of the path. While this facilitates the interpretation of the measurements because source side contributions are eliminated, the known polarization makes the detection of anisotropy less ambiguous. Because this phase arrives with near vertical incidence at the receiver, it is sensitive to azimuthal anisotropy.

Approximately 90 per cent of the stations reviewed by Silver (1996) show anisotropy detected by *SKS* splitting, with splitting times that range from 0.5 up to 2 s with an average around 1 s. Assuming 4 per cent anisotropy and a shear wave velocity of 4.5 km s^{-1}, 1 s of splitting time corresponds to a thickness of the anisotropic layer of approximately 110 km. Splitting times resulting from anisotropy in the crust are mostly lower than 0.2 s, while those attributed to the lower mantle are assumed to be smaller than 0.2 s (Savage 1999, and references therein). Consequently it is probable that splitting times above 0.5 s are caused by the upper mantle. However, as a result of the vertical incidence of *SKS*, there is no direct way to determine the depth distribution of anisotropy with these phases alone.

2.1 Method

We determine splitting parameters using the method described by Silver & Chan (1991). The splitting parameters obtained are the azimuth of the fast axis, Φ, and the splitting time δt, which is the delay between the arrival of the fast and slow component of a shear wave. One either searches for Φ and δt that will result in the most linear particle motion on the unsplit traces or alternatively for the parameters that most successfully remove the energy on the transverse component of the unsplit traces, which is more straightforward for *SKS*.

An advantage of the method of Silver & Chan (1991) is that formal errors are calculated. These formal errors are independent of signal-to-noise (S/N) ratio and thus only meaningful if actually a signal is measured. The unsplitting of noise can result in a non-null, but meaningless measurement with a small formal error. Therefore, we measured *SKS* splitting only for seismograms with a good S/N ratio.

In the case of one anisotropic layer of hexagonal symmetry (transverse isotropy) with a horizontal fast axis, the splitting parameters depend weakly on initial polarization (eg. backazimuth in the case of *SKS*), because of the non-vertical incidence. If anisotropy is heterogeneous, a stronger dependence on initial polarization is expected. Following Silver & Savage (1994), splitting parameters obtained under the assumption of one anisotropic layer when in fact anisotropy is more complicated, are called apparent splitting parameters. Two anisotropic layers with different azimuths of the horizontal fast axes, will cause a 90° periodicity of the apparent splitting parameters. An inclined symmetry axis will also cause azimuthal variations, as does the presence of more complex symmetry systems. The assumption of a hexagonal symmetry system has been confirmed from measurements of subcontinental rock samples (Mainprice & Silver 1993).

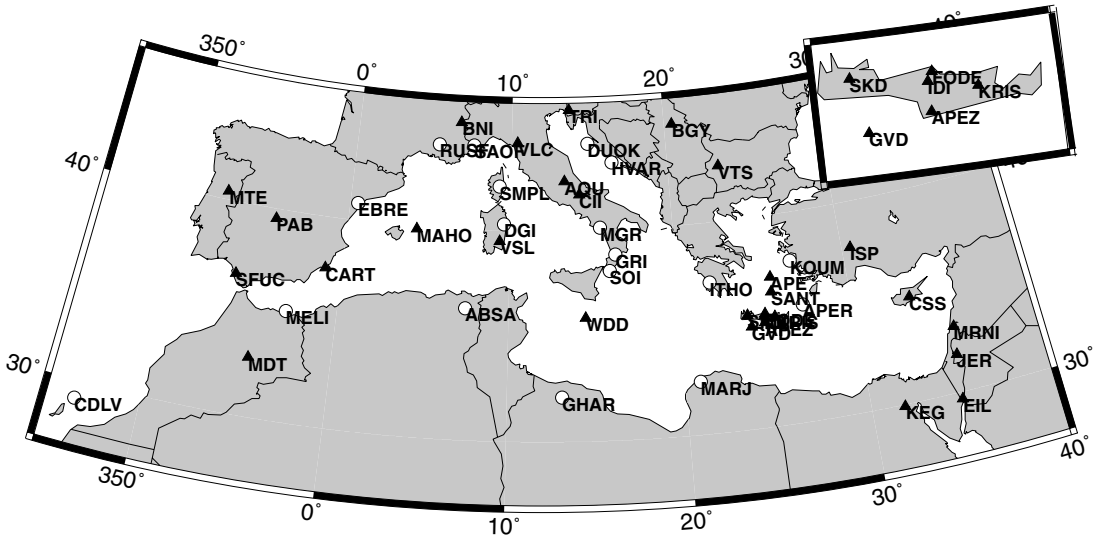

Figure 2. Map showing location of stations used in this study. Open circles give location of MIDSEA stations, stations from permanent networks are shown by the triangles.

2.2 Data

We use broad-band data from the temporary MIDSEA network (Van der Lee *et al.* 2001) and additional data from permanent stations of the GEOFON (Hanka & Kind 1994) and MedNet (Boschi *et al.* 1991) networks. Fig. 2 shows the locations of the stations that were used here and/or in the remainder of the paper. We collected seismograms from earthquakes that occurred in a distance larger than 85° and that had a magnitude ≥6. The earthquakes are shown in Fig. 3. From those we selected seismograms with *SKS* arrivals with a signal to noise ratio (S/N) over 3, which is estimated from the SKS signal and 20 s of noise immediately preceding *SKS*. Seismograms for which the *SKS* particle motion was considered elliptical were used to measure splitting. Some seismograms did not show a split *SKS* and yield a so-called null measurement, which occurs when the underground is isotropic or when polarization direction of the incoming shear wave is identical with either the slow or fast axes of symmetry. In Fig. 4 an example is shown of our *SKS* splitting analysis for an event in the western Pacific, recorded at MIDSEA station DGI.

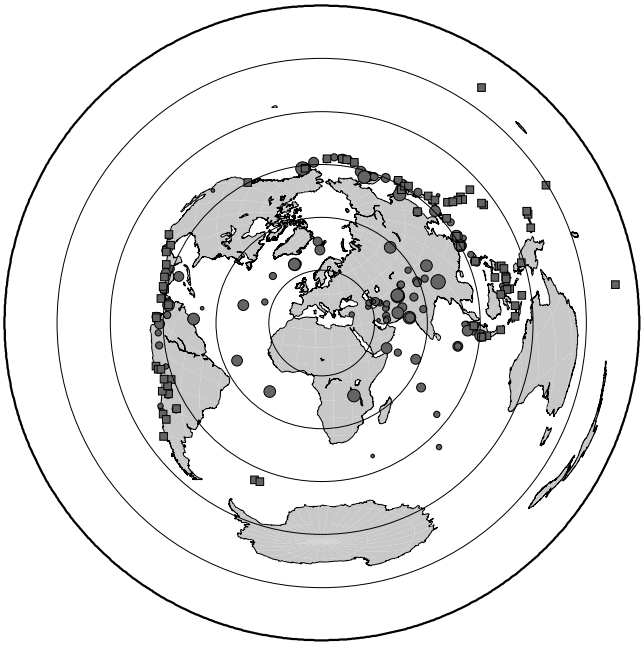

Figure 3. Map showing source locations of events used in this study. Events used for the splitting analysis are shown with squares while circles give events used for *P* delay measurements, size of circles is proportional to the number of stations where delays could be measured. Large circles show distance to the centre of the study region with increments of 30°.

2.3 Results

A map showing all splitting parameters that were obtained is given in Fig. 5. The weighted mean values of the splitting parameters are given in Table 1 and displayed in Fig. 6. We use the following definition to calculate the mean values for one station:

$$\overline{t} = \sum_{k=1}^{N} w_k t_k, \tag{1}$$

where t is the splitting time and N is the number of non-null events. The weights w_k are defined by

$$w_k = \left(1/{\sigma_k}^2\right) \Big/ \left(\sum_{i=1}^{N} 1/{\sigma_i}^2\right), \tag{2}$$

with σ_i being the formal error of the ith measurement. The error in the mean splitting time is estimated by the weighted average variance

$$\tilde{\sigma}^2 = \frac{N}{N-1} \sum_{k=1}^{N} w_k (t_k - \overline{t})^2. \tag{3}$$

We apply directional statistics (Mardia & Jupp 2000) to calculate the weighted average fast axis orientation, which is then given by

$$\overline{\theta} = \begin{cases} \tan^{-1}(\overline{S}/\overline{C}) & \text{if } \overline{C} \geq 0 \\ \tan^{-1}(\overline{S}/\overline{C}) + \pi & \text{if } \overline{C} < 0 \end{cases}, \tag{4}$$

with $(\overline{C}, \overline{S})$ being the weighted mean of the centre mass

$$\overline{C} = \sum_{k=1}^{N} w_k \cos\theta_k \qquad \text{and} \qquad \overline{S} = \sum_{k=1}^{N} w_k \sin\theta_k, \tag{5}$$

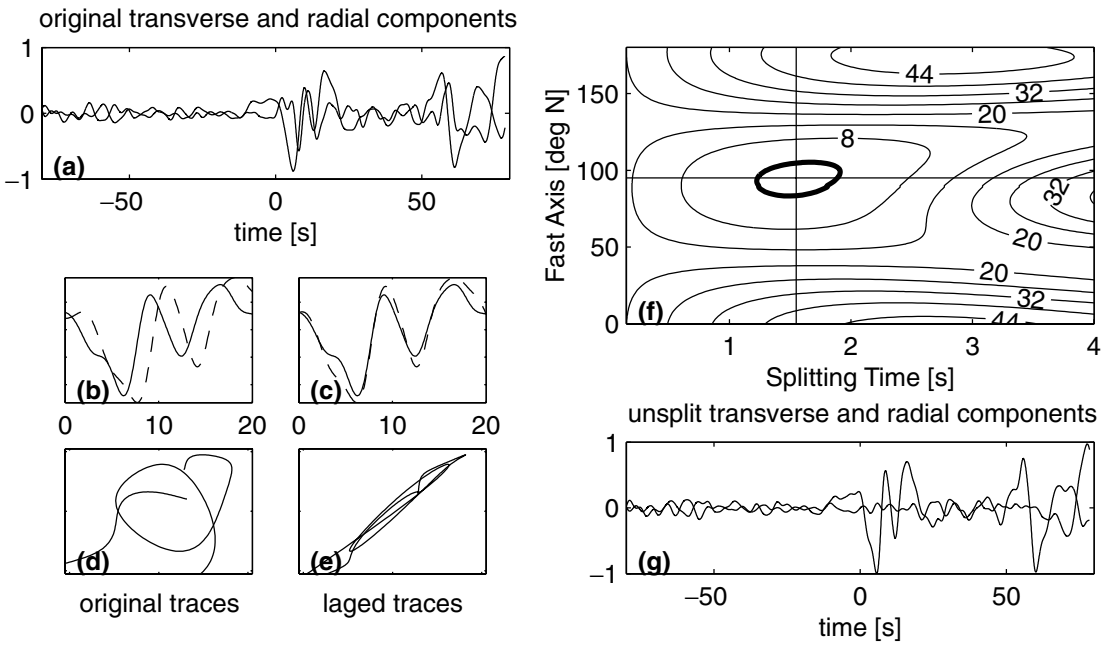

Figure 4. Example of the splitting analysis for the 2000 March 28 (day 88) Volcano Island event recorded at DGI, Sardinia. (a) Original horizontal components of the seismograms, zero time corresponds to the predicted onset of *SKS*, (b, c) original and time-shifted traces and the associated particle motions (d, e), all rotated into the fast/slow axis frame. The shown time window is the same as was used for the splitting analysis. (f) Shows the result of the grid search for the best-fitting splitting time, $\delta t = 1.60s$ and fast axis orientation, $\Phi = 93^{\circ}$N. Contours are labelled with the level of standard deviation at which parameters match the observations. Thick contour line represents two standard deviations and thus the 95 per cent confidence interval. (g) Seismograms corrected for the estimated splitting, *SKS* energy on the transverse component has been successfully removed.

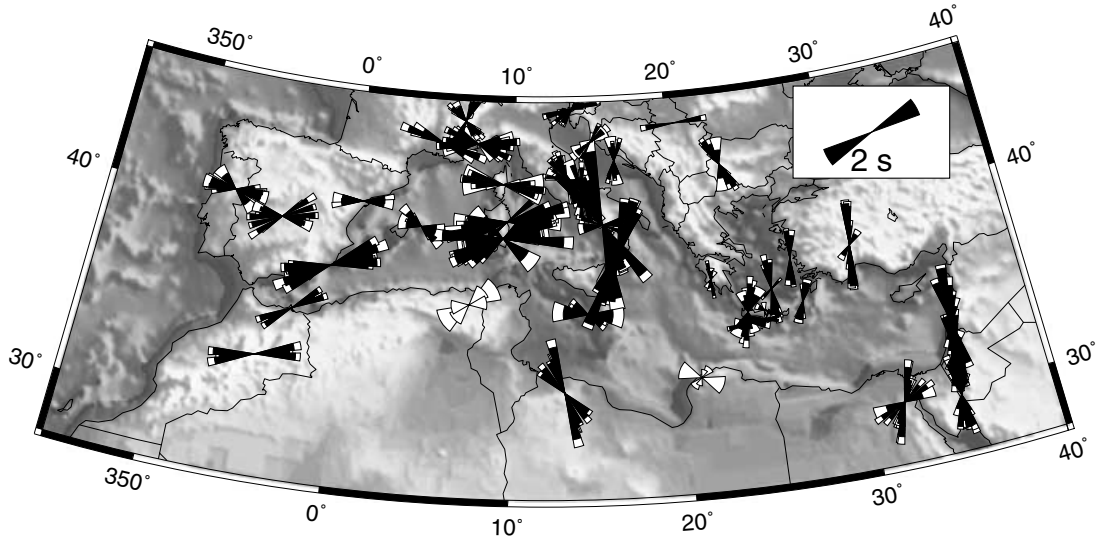

Figure 5. Map showing splitting parameters that were derived in this study. Wedge width is proportional to the standard deviation of the fast axis direction, white areas at the outside of the wedges are proportional to the standard deviation of the splitting time. The thick black line shows the different domains of anisotropy, as discussed in the text.

with the same weights as in eq. (2). For the definition of the circular standard deviation we use

$$v = -2\log\overline{R} \qquad \text{with} \qquad \overline{R} = (\overline{S}^2 + \overline{C}^2)^{1/2}, \tag{6}$$

where $\overline{R}$ is the mean resultant length.

2.3.1 *On the observed dependencies on frequency*

As for most seismic stations, the S/N ratio of our data depends on the frequency band under consideration. If possible, we measure splitting from the unfiltered traces as well as from the following passbands: 10–50, 3.3–33, 1–20 and 1–12.5 s. The dominant period of *SKS* is around 8–10 s, which is similar to the dominant period of noise at island stations. We further tested, if our data show a dependence of the splitting parameters on frequency, such as observed by Marson-Pidgeon & Savage (1997). They showed measurements for a station in New Zealand where large discrepancies between *SKS* and shorter period *ScS* were observed. Numerical investigations of wave propagation in heterogeneous anisotropic media (Rümpker &

Table 1. Mean value of splitting parameters for stations with more than one observation.

Station name	Num. obs.	δt	$\tilde{\sigma}$	Φ	v
ABSA	3	1.03	0.33	58.38	15.61
APER	4	0.83	0.07	19.03	2.97
APEZ	5	0.52	0.11	87.03	27.28
AQU	11	0.98	0.12	−35.36	20.27
BGY	1	1.30	0.23	87.00	10.00
BNI	6	0.97	0.17	−30.59	36.89
CART	10	1.72	0.20	69.81	9.21
CII	4	1.21	0.16	−6.37	12.21
DGI	11	1.56	0.38	80.93	11.82
DUOK	5	0.61	0.23	45.34	11.96
EBRE	4	0.92	0.16	85.87	7.56
EIL	12	1.33	0.14	3.02	7.79
FODE	1	0.45	0.15	120.00	17.00
GHAR	7	1.42	0.19	−27.48	12.77
GRI	6	1.95	0.26	22.19	5.96
GVD	3	0.91	0.16	87.77	8.38
HVAR	6	0.74	0.11	9.23	11.57
IDI	1	0.40	1.33	3.00	14.50
ISP	5	1.46	0.44	10.85	12.48
ITHO	4	0.57	0.19	4.78	14.35
JER	9	1.36	0.22	8.03	9.00
KEG	14	1.01	0.30	32.80	19.58
KOUM	3	1.05	0.16	1.66	3.78
KRIS	0	–	–	–	–
MAHO	4	0.68	0.14	120.36	13.17
MARJ	3	0.52	0.29	46.00	42.46
MDT	3	1.62	0.19	77.34	5.75
MELI	3	1.39	0.07	55.68	5.81
MGR	18	1.37	0.64	−27.46	19.77
MRNI	8	1.53	0.54	7.05	8.56
MTE	8	1.03	0.17	89.63	14.17
PAB	7	1.25	0.18	74.50	21.59
RUSF	2	1.64	0.29	110.23	1.48
SANT	6	0.76	0.35	9.10	28.12
SAOF	11	1.30	0.19	94.07	13.48
SFUC	0	–	–	–	–
SKD	7	0.70	0.36	12.45	10.89
SMPL	5	1.54	0.19	94.70	8.54
SOI	1	2.53	0.18	26.00	10.00
TRI	10	0.73	0.20	55.64	18.57
VSL	24	1.64	0.37	69.13	13.27
VTS	8	0.96	0.22	−26.36	6.55
WDD	5	0.83	0.15	115.40	11.08

Silver 1998; Rümpker *et al.* 1999; Saltzer *et al.* 2000), also predict a dependence of the splitting parameters on frequency.

Just in a small number of cases it was possible to determine reliable splitting parameters in each of the aforementioned frequency bands. Most arrivals with a high S/N ratio gave virtually identical results for passbands of 3.3–33 and 1–20 s, which is not surprising because both bands include the dominant period of *SKS*. Splits measured in the 10–50 s band sometimes gave larger splitting times, but with a grid search showing elongated banana shaped minimas indicating large trade-offs, therefore the number of significant results is too small to draw meaningful conclusions about the frequency dependence. The same observation was made for the 1–5 s passband, where S/N was mostly too low to make a measurement.

2.3.2 *Description of results*

The general pattern of observed anisotropy is relatively homogeneous (Fig. 6). In the western Mediterranean a dominant E–W alignment of the fast direction is evident (Fig. 6). The pattern of anisotropy is different for the Italian peninsula, with a fast axis that is relatively N–S, which confirms recent observations by Margheriti *et al.* (2003). Stations on the east coast of the Adriatic sea show small splitting times, a trend that continues along the Aegean trench. Stations further east again show well developed splitting, with N–S directed fast axes. Azimuthal anisotropy is also found in northern Africa, with a fast axis alignment approximately NE–SW for most stations.

From two (SFUC and KRIS) of the 43 stations listed in Table 1, we solely obtained null measurements. The S/N ratio at 8–10 s at island station CDLV was generally too high to perform splitting measurements.

2.3.3 *On station misorientations*

Splitting parameters are determined using both modes, minimizing energy of the transverse component as well as finding the most linear particle motion on the unsplit traces. In the ideal case, results will be identical for both methods and the polarization vector determined from the second method will be equal to the backazimuth. Systematic discrepancies between the measured unsplit polarization and the back azimuth is likely caused by station misorientations. These are not uncommon, as is evident for example from the studies of Laske (1995) or Schulte-Pelkum *et al.* (2001), who report misorientations of up to 25°. Three stations appear to be misoriented. These are listed in Table 2, and the shown fast axes orientations in Table 1 and Figs 5 and 6 are corrected for these estimated misorientations. Note that lateral heterogeneities such as dipping layers may also cause a discrepancy, which however depends on back azimuth.

2.3.4 *Variations with back azimuth*

Because the splitting parameters vary with initial polarization if anisotropy is heterogeneous, the calculation of mean values can be misleading. However, if data coverage is limited, we still think it is useful to calculate these averages in order to get a first-order estimate on anisotropy. For example, in the case of two anisotropic layers, when the fast axis azimuths are not too different (<45), the average value of the apparent fast axis azimuths will be close to the average fast axis azimuth of the two layers, while the average of the apparent splitting times is equal to the sum of the splitting times of the two layers (Rümpker & Silver 1998).

There are stations that show a variation in the splitting parameters exceeding the standard deviation as estimated by the splitting analysis. However, none of the stations has sufficient azimuthal coverage to resolve a potential azimuthal periodicity and to assign it to a specific cause such as multiple anisotropic or dipping layers.

2.4 Discussion

2.4.1 *Relation between splitting measurements and tectonics*

Lattice preferred orientation of anisotropic olivine crystals is widely accepted as the main cause of anisotropy in the upper mantle. There is more debate about the dominating geodynamical process that causes the finite strains leading to lattice preferred orientation. Silver (1996) discusses the two end member explanations for continental mantle anisotropy, which are simple asthenospheric flow and vertically coherent deformation. For simple asthenospheric flow, it is assumed that the source of anisotropy is in a decoupled zone of the

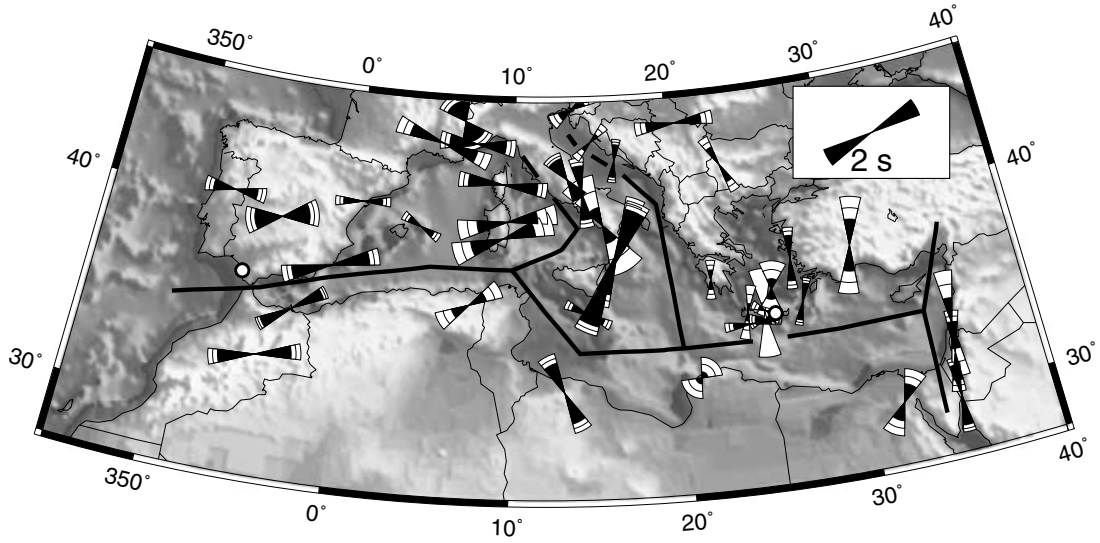

Figure 6. Map showing mean values of the splitting parameters as given in Table 1. Dots give stations where splitting was not observed.

Table 2. Observed stations misorientations.

Station name	Angle (°)	Sense
APER	20	↶
VSL	20	↷
MAHO	10	↶

asthenosphere as a result of the movement of the lithosphere over the stationary deeper mantle. Vertically coherent deformation assumes coherent deformation of the crust and lithosphere during tectonic events; with subsequent cooling, the anisotropic fabric may be preserved for long periods of time until another tectonic event overprints it. Cooling is necessary in order to preserve the anisotropic fabric. The critical temperature is around 900 °C (Savage 1999); lower temperatures are required to preserve the fabric, but higher temperatures are needed to efficiently orient the minerals.

Coherent splitting parameters over large regions are the main diagnostic for simple asthenospheric flow, while vertically coherent deformation can show large variations over short spatial scales. These are end members and in reality often both mechanisms may be at work alongside. The sensitivity of the shear splitting analysis is larger for shallow layers than for deeper layers (Saltzer *et al.* 2000). Therefore, lithospheric anisotropy may hide in many cases a possibly ubiquitous deeper source of anisotropy.

At convergent margins, the anisotropy may be caused by mantle flow induced by the descending slab and more complex patterns of anisotropy will form (Vinnik & Kind 1993; Russo & Silver 1994; Gledhill & Gubbins 1996). An additional contribution may arise from pre-existing anisotropy inside the slab.

Given a process for producing anisotropy, clear predictions about the observed fast axis directions can be made. Simple shear will lead to a dominant fast axis orientation of the shear plane minerals parallel to the direction of shear. Extension should result in a fast axis orientation parallel to the direction of extension (Silver 1996). Uniaxial compression is expected to lead to a fast axis orientation parallel to strike of structures, most likely a result of the preferred alignment of the slow axis in the direction of shortening (Savage 1999). In fact, in many cases the observed fast axis direction follows the trend given by the mountain belts (Silver 1996).

In the case of simple asthenospheric flow, the fast axis will be aligned parallel to the absolute movement of the lithosphere. The time needed to align the minerals in the direction of infinite strain is of the order of several million years (Kaminski & Ribe 2002).
It is evident that for a complex region such as the Mediterranean no unique model will explain all observations. In the next section, we try to explain the relative importance of the above models in various parts of the Mediterranean.

2.4.2 Proposed models of anisotropy for the Mediterranean region

Because the fast axis shows a consistent pattern in several domains, we first compare the fast axis directions with the absolute plate velocities for the Mediterranean region, shown in Fig. 1.

To derive these absolute velocities we used the relative velocities of Bird (2003) and linked them into the hotspot reference frame via the finite reconstruction pole of Africa as given in Müller *et al.* (1993). Fig. 7 shows a histogram of the difference between the

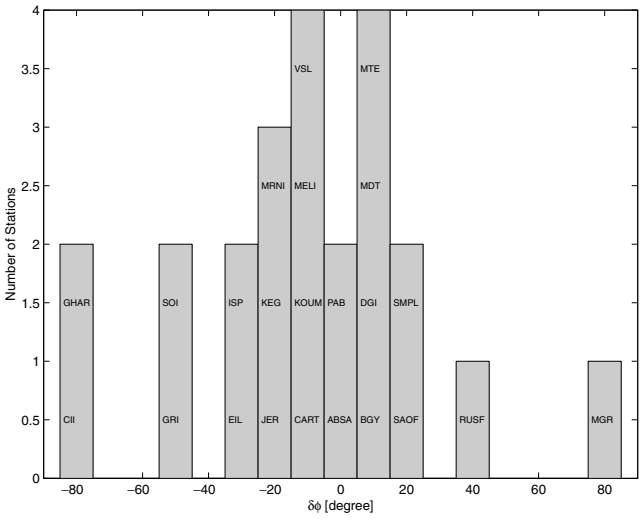

Figure 7. Histogram of difference between the azimuth of the fast axis of anisotropy Φ and the azimuth of absolute plate motion Φ_{APM}.

absolute plate motion azimuth and that of the azimuth of the fast axis of anisotropy. Using a χ^2 test, we can conclude that the observed distribution is different on the 95 per cent level to one expected from a uniform distribution. This histogram does not change significantly when we use the REVEL model of Sella *et al.* (2002), which shows plate motions relative to the ITRF-97 reference frame.

If simple asthenospheric flow is an important contribution to the observed anisotropy, we expect the values of the difference to scatter around zero, which is in fact seen in Fig. 7. Most outliers can be associated with subduction zones or locations of non-rigid behavior (see Figs 1 and 6). A good correlation is found for the stations in the western part, as well as for the stations in the east. In North Africa we also see a good correlation, with the exception of station GHAR. Based on this observation, we divide our observations loosely into five domains, inside which anisotropy shows characteristic features.

As a first domain, we define the part of Eurasia in the west where anisotropy aligns with plate motion and can thus be explained by the simple asthenospheric flow model. Even though plate velocities are not high, their directions have been steady. The time required to develop strain-aligned anisotropy from initial isotropy is inversely proportional to the strain rate (Kaminski & Ribe 2002). If strain is maintained over a long period of time [O(10 Myr)], anisotropy will align with deformation even if the strain rate is low.

The stations on Sardinia (DGI, VSL) and Corsica (SMPL) also fit in this first domain, even though the situation is likely more complex as indicated by the large splitting times. The directions of lithospheric extension in the recently formed basins surrounding these islands are roughly parallel to the motion of the Eurasian plate, especially for the Tyrrhenian sea. We attribute the splitting observations at least in part to mantle flow accompanying this extension.

Results of *SKS* splitting analysis at station VSL were recently presented by Margheriti *et al.* (2003). They report a dependence of the splitting parameters on initial polarization, which they attribute to two anisotropic layers, a shallow one and another resulting from a subhorizontal, flat-lying slab above the mantle transition zone at 660 km. We also observe some scatter in the splitting measurements at VSL, but much less for neighbouring station DGI. We cannot find a satisfactory fit to our measurements using the two layer model of Silver & Savage (1994). To explain the scatter, we prefer the simpler explanation of alignment with eastward directed plate-motion related mantle strain and a possible process of reorienting mantle crystals into the more southeasterly direction of opening of the Tyrrhenian sea.

The second domain, stations along Northern Africa, can also be explained by simple asthenospheric flow related to absolute motion of the African Plate, with the exceptions of stations GHAR and WDD. Although the MIDSEA project substantially improved data coverage in northern Africa, we feel that it must be further improved to fully explain this anisotropic pattern.

For both of the above domains, an explanation in the context of vertically coherent deformation is also possible, because many of the stations show an orientation that is parallel to the trend of mountain belts. For example observations along the east coast of Spain (EBRE, CART) and Africa (MELI, ABSA) can be related to compressive deformation in the past. Subduction was directed NNW before 30 Ma and the average fast axes directions are roughly perpendicular to this direction. This would explain splitting at Balearic Island station MAHO as well. Around 30 Ma, this island was still attached to the Iberian peninsula and the observed clockwise rotation of the fast axis relative to the Peninsula fast directions coincides with the estimated rotation encountered by the Balearic islands during the opening of the Valencia trough (Dercourt *et al.* 1986), which moved this island to the present location after the NNW compression.

More enigmatic is the behavior of stations that are located in the vicinity of active subduction zones. Active subduction is currently taking place along the Calabrian and Hellenic arcs (McKenzie 1970; Wortel & Spakman 2000).

We define a third domain that contains the measurements from the Italian peninsula and Sicily. The fast axes are parallel to the arcuate (Apenninic) mountain belt and thus to the strike of recently (central Italy) and currently (southern Italy) subducting lithosphere. Especially the stations along the Calabrian arc show large splitting times, in fact the numerous splits around 2 s are the largest that we observe in the Mediterranean region. Splitting times that are large imply either an anomalously high level of anisotropy or an anisotropic layer with a thickness extending 200 km. According to the Wadati–Benioff zone and tomographic models (Piromallo & Morelli 2003), the slab has a steep dip. Our stations sample mantle below and above the slab. A comparison with seismicity shows that we are sampling at least 150 km of the mantle above the slab. One explanation for the observed high splitting times and directions may be trench-parallel mantle inflow above the slab (Gvirtzman & Nur 1999) or mantle outflow below the slab (Russo & Silver 1994). Gvirtzman & Nur (1999) discuss a relatively shallow and recent (<0.5 Ma) event, likely too recent to be capable of aligning mantle minerals in the direction of flow. Another explanation is that pre-existing anisotropy in the downgoing oceanic lithosphere in combination with the steep dip of the slab might cause the large splitting times. However, as a result of the different path lengths inside the subducting slab, large variations of the splitting times with backazimuth should be observed, which is not the case. A third explanation may be found in the presence of water. The lattice preferred orientation of olivine changes with the addition of water and will result in a different seismic signature (Jung & Karato 2001). Under dry conditions, the expected fast axis direction resulting from corner flow is parallel to the direction of subduction. The supply of water from the downgoing lithosphere may change this pattern and result in a fast axis direction parallel to the trench, which would be in agreement with our observations.

The central Italian fast directions parallel to the mountain belt are either caused by alignment of the slow axis in the direction of compression or may alternatively be caused by the corner flow in a hydrated mantle wedge. Note that the trench-parallel fast axis directions agree relatively well with fast axis directions estimated from *Pn* tomography (Hearn 1999), which is more sensitive to shallow anisotropy than is *SKS* splitting.

As the next domain, we define the vast region between stations TRI and ISP, where mostly small splitting times, with $\delta t < 1s$ are observed. Stations in vicinity of the Dinarides show small splitting with a fast axis that is atypically not parallel to the mountain belt but almost perpendicular it. As a result of the small splitting times, one may be inclined to attribute anisotropy to a shallow origin, however a deeper origin may be equally likely.

The stations on Crete and nearby islands show little anisotropy with a badly defined fast axis or even no anisotropy at all. It is somewhat surprising that anisotropy is not present beneath these stations because slab roll-back in the Aegean is relatively strong (Meijer & Wortel 1997) and we might expect significant anisotropy to be present as a result of the induced mantle flow. One explanation is that, as a result of the close proximity of the slab, anisotropy is too heterogeneous to be measured under the assumption of a single anisotropic layer. The heterogeneity causes a shift into the domain characterized as strong incoherent scattering by Saltzer *et al.* (2000).

Stations further north and farther away from the trench show a better defined splitting, as was observed also by Hatzfeld *et al.* (2001). The observed N–S directions are in accord with backarc extension and with the approximate absolute movement of Aegean microplate. Both mechanisms can explain the observed splitting times and based on our measurements we cannot distinguish between the two.

Finally, we define a domain that includes the three easternmost stations, located along the Dead Sea rift. Here the fast axis orientation is parallel to the Dead Sea rift and to the relative plate motion between Arabia and Africa and can be explained by current vertically coherent deformation caused by the strike slip motion between the two plates. The relative motion of the two plates is very close to their absolute motion and a contribution to the observed splitting from the asthenosphere is also likely.

3 TELESEISMIC DELAY TIMES

In the previous section, we established the widespread presence of anisotropy in the Mediterranean area. Here we measure delay times of teleseismic body waves and investigate whether they are affected by this anisotropy through studying the dependence of the delay times on backazimuth (Dziewonski & Anderson 1983) and comparing the delay times to synthetic delay times computed for the anisotropy documented in the preceding.

3.1 Data

We measure relative arrival times of teleseismic *P* and *S* waves. Approximately 160 teleseismic events in the period from 1997 to 2001 were analysed and are mapped in Fig. 3. We use data from the MIDSEA, GEOFON and MedNet networks (Fig. 2).

Interstation relative delay times are measured using the multichannel cross-correlation method (MCCC) of VanDecar & Crosson (1990). For a given event, this method first determines the time-shift associated with the maximum of cross-correlating the body waveforms for each station pair. In a second step, an optimized set of relative delays with zero mean is obtained by least squares inversion of the overdetermined system that resulted from the first step. In total, we have measured ∼2000 relative *P* arrivals and 900 relative *S* arrivals of teleseismic events from the distance range 30°–90°. *P* measurements are taken from the vertical component, while the transverse component was used for *S*.

From the measured relative delays, we calculated azimuth-dependent station statics. The methodology and the results are discussed in detail in Sections 3.3 and 3.4, respectively.

3.2 Frequency dependence of delay measurements

In upper-mantle traveltime tomography, relatively high-frequency delay times are generally inverted for velocity anomalies with length scales as large as a few hundred kilometres. This is justified when the used body waves are not dispersed. However, the sensitivity of seismic body waves to velocity heterogeneities changes with the wavelength of the wave. Before systematically measuring delay times, we investigate their dependence on the filtering frequencies that we use in the cross-correlation procedure. We would like to know whether delays measured in different frequency bands represent the same velocity structures.

To do so, we selected two pairs of events, given in Table 3. The hypocentres of the two events in each pair are close. We then cross-correlate the *P* body waveforms for each event using a series of bandpass filters with overlapping frequency bands. We choose the overlapping passbands to be as narrow as possible, while maintaining a clearly visible arrival. This cross-correlation procedure produces frequency-dependent relative delay time measurements. Uncertainties in these delay times were estimated by remeasuring the delays with slightly perturbed filtering parameters.

Fig. 8 compares the resulting relative delays as a function of frequency. A variation with frequency of the delays is observed at most stations. The event pairs show similar delay and frequency

Table 3. Earthquake pairs used for determination of frequency dependence. Source locations from Engdahl *et al.* (1998).

	Event	Time	Latitude (°N)	Longitude (°E)	Depth (km)
1A	1999:312	16:45	36.48	71.23	222.2
1B	2000:199	22:53	36.20	70.98	136.7
2A	1999:258	03:01	−20.78	−67.22	212.1
2B	2000:133	18:43	−23.78	−66.78	234.4

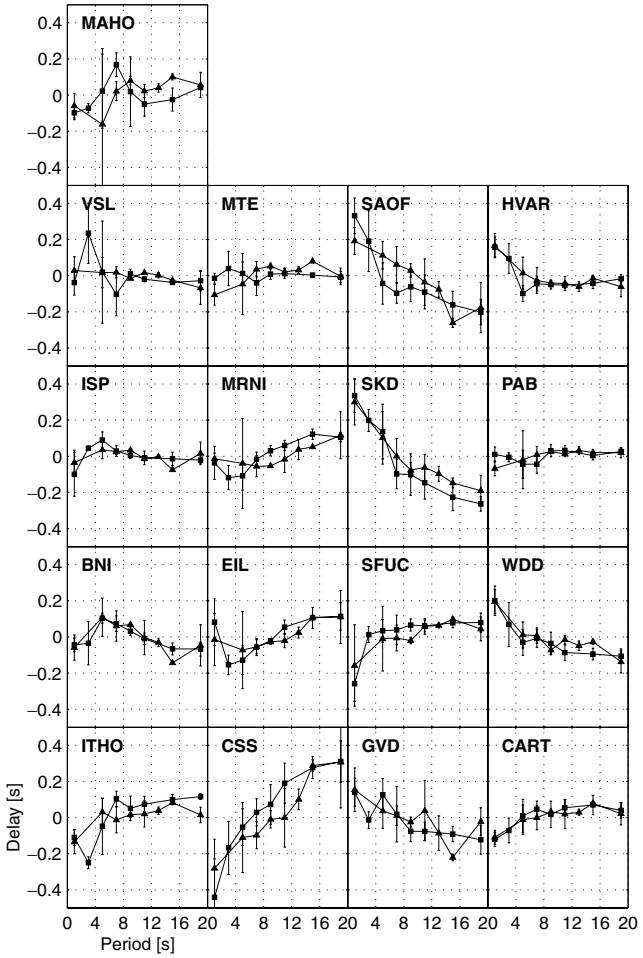

Figure 8. Comparison of relative delays as a function of the filtering frequency used in MCCC, (a) for two closely located events (event 1A vs 1B, see Table 3), (b) as (a) except 2A vs 2B and (c) two distant events (1A vs 2B). In all cases, only stations are considered that recorded both events. In order to stabilize the result, events were measured several times with different window lengths in MCCC. Then the measurements were binned in 2-s windows according to the midpoint between the corner frequencies and finally the station mean was removed. Error bars range from the maximum to the minimum value inside the bin.

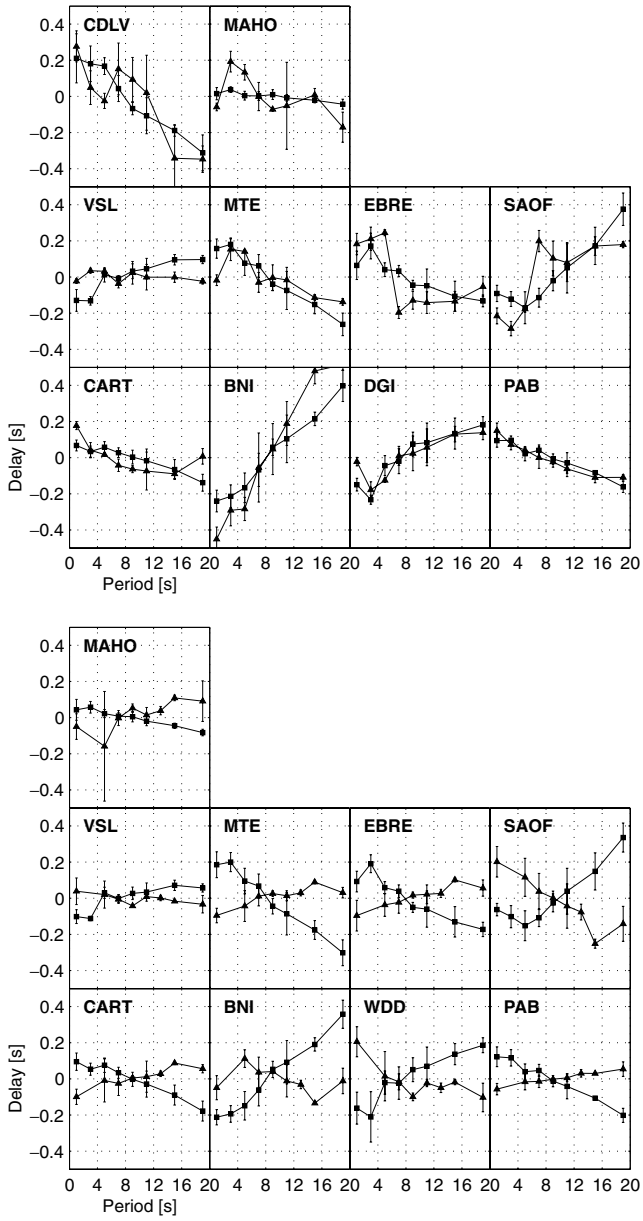

Figure 8. (*Continued.*)

dependencies (Figs 8a and b), thus showing that the variations are not the result of noise. Furthermore, the delays and frequency dependence are different for events with different locations (Fig. 8c), indicating that we are not measuring a receiver effect such as crustal reverberations. The observed frequency dependence is a few tenths of a second and seems significant for many stations even though for most stations the amplitude of the variation is only slightly larger than the standard deviations of the measurements, suggesting that we cannot reject the common assumption that they are independent of frequency.

The frequency dependence of traveltime sensitivity kernels can cause the observed frequency dependence of the delay times if the size of velocity anomalies is in the range where diffraction has a significant influence on the delay time. Our observations are for frequencies between 0.05 and 1 Hz, corresponding to wavelengths of approximately 10 to 200 km, when assuming an upper-mantle P velocity of the order of 10 km s^{-1}. For diffraction effects to be of importance, heterogeneities with scale lengths on the same order as the wavelength are required (Müller *et al.* 1992; Tong *et al.* 1998). In this case, the apparent delay time can be up to 50 per cent different from the maximum ray theoretical delay time (Tong *et al.* 1998). The frequency dependence we observe is a few tenths of a second (Fig. 8), which is in general much less than 50 per cent of the observed delay times (Fig. 9a). While the observed dependence of delay times on frequency confirms that in the Mediterranean region heterogeneous upper-mantle structure exists on scale lengths between 10 and 200 km, the fact that this frequency dependence is slight implies (Tong *et al.* 1998) that heterogeneity on scale lengths near and over 200 km dominates. This, and the fact that we generally cannot reject the hypothesis of no frequency dependence, is encouraging in view of the validity of high-frequency delay time tomography, which images structures on these scales.

3.3 Azimuth-dependent time term analysis

We perform a classical time term analysis (i.e. Cleary & Hales 1966)

The absolute arrival time of a seismic phase can be written as the sum of an expected arrival time, given by the reference model, and a delay time,

$$t_{\rm obs} = t_{\rm ref} + \delta t. \tag{7}$$

The delay time can further be written as,

$$\delta t_{ik} = s_i + a_{ik} + e_k, \tag{8}$$

where indexes i and k represent station and earthquake, respectively. s is the station term, a the path term and e the event term.

The station term should absorb station elevation and the crustal structure, including thickness and sediments. Errors in event location and origin time are included in the event term. The path term includes the effects of 3-D deviations of seismic velocities relative to the reference model and the ellipticity of the Earth. Because the paths for each event are closer to each other near the source than near the receiver, the path term is dominated by receiver side contributions and most of the source side heterogeneity is absorbed by the event term.

We correct for ellipticity (Dziewonski & Gilbert 1976). Because elevation, crustal thickness and sedimentary thickness are relatively well known, we attempt to predict and remove the station term from eq. (8) by subtracting it from both sides. We use the Moho map of Marone *et al.* (2003) and sediment thicknesses from the crustal model CRUST 2.0 of Bassin *et al.* (2000) to make these corrections.

After these corrections, the delay time then becomes,

$$\delta t_{ik} = d_{ik} + e_k, \tag{9}$$

with d_{ik} as defined by (Dziewonski & Anderson 1983):

$$d_{ik} = \sum_{n=0}^{N} (A_{in} \cos n\xi_{ik} + B_{in} \sin n\xi_{ik}), \tag{10}$$

where ξ_{ik} is the backazimuth of station i to earthquake k.

In the cross-correlation analysis we determined relative times and we can write an interstation relative delay time as:

$$\delta t_{ijk} = t_{ik} - t_{jk} - \delta t_{{\rm ref},ijk} = d_{ik} - d_{jk}, \tag{11}$$

where $\delta t_{{\rm ref},ijk}$ is the difference in expected arrival times from the 1-D reference model. We use the AK135 reference model of Kennett *et al.* (1995). We assume that the source term e is the same for both stations. This approximation is justified as long as the two

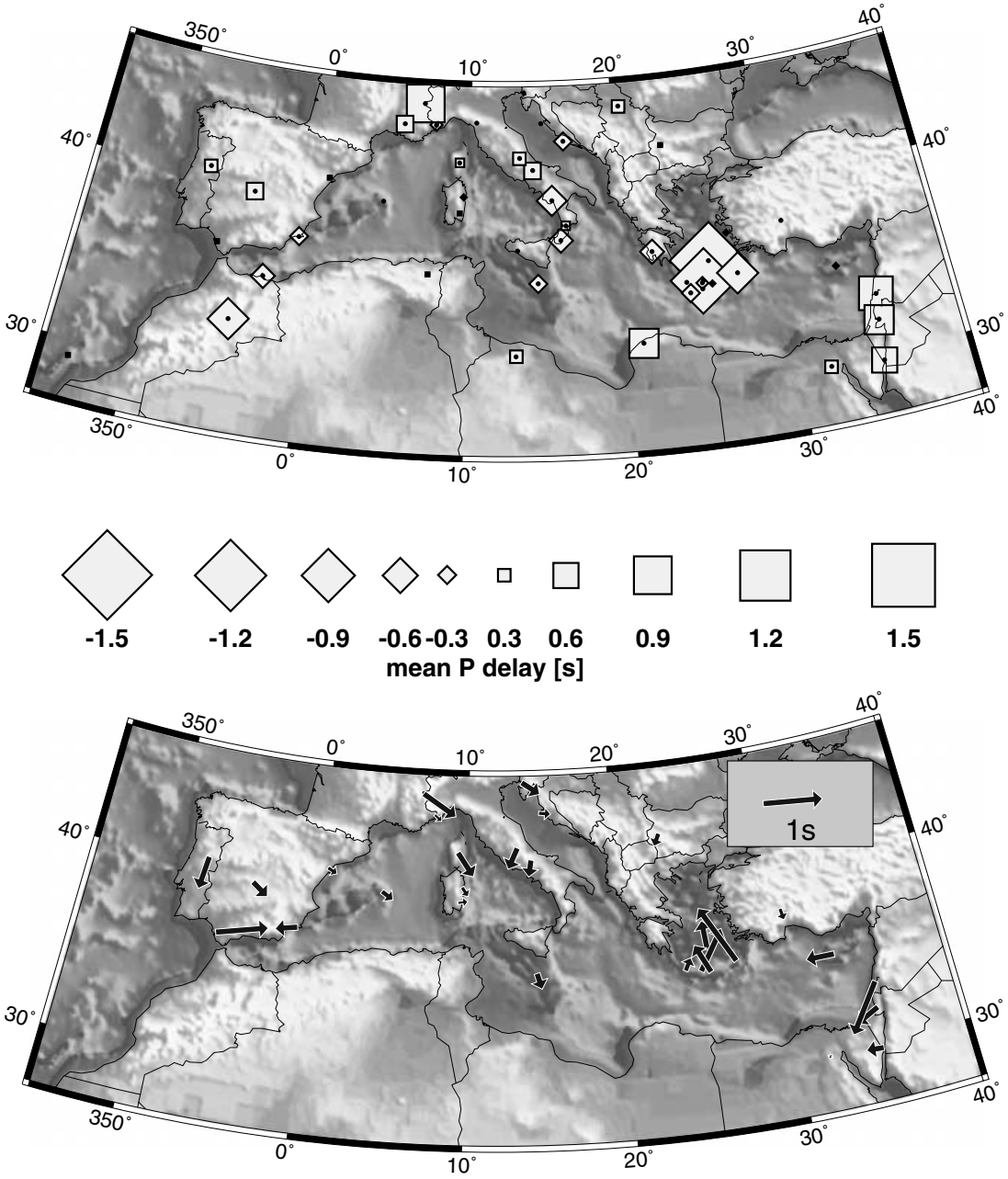

Figure 9. (a) Map of the static P term, which images larger scale isotropic velocity heterogeneity. (b) Map of the first azimuthal P term. No relation to the fast directions determined from the *SKS* splitting analysis is apparent, instead this term appears to be dominated by lateral variation beneath the stations. (c) Map of the second azimuthal P term. Unlike the first azimuthal term shown in Fig. 9(b), the second azimuthal term is related to anisotropy.

stations are relatively close. We expand the azimuthal term to second order,

$$\begin{aligned} d_{ik} - d_{jk} = {} & A0_{ik} + A1_{ik}\cos\xi_{ik} + B1_{ik}\sin\xi_{ik} \\ & + A2_{ik}\cos 2\xi_{ik} + B2_{ik}\sin 2\xi_{ik} \\ & - A0_{jk} - A1_{jk}\cos\xi_{jk} - B1_{jk}\sin\xi_{ik} \\ & - A2_{jk}\cos 2\xi_{jk} - B2_{jk}\sin 2\xi_{ik}, \end{aligned} \tag{12}$$

which can further be written in compact form as a system of equations,

$$\mathbf{d} = \mathbf{Am}. \tag{13}$$

The data vector **d** contains the interstation relative delay times, the model vector **m** the A and B terms from eqs (10) and (12) for every station. The non-zero elements of the matrix **A** contain either ± 1 corresponding to the $A0$ terms, $\pm\cos\xi$ ($\sin\xi$) for the $A1$ ($B1$) terms or $\pm\cos 2\xi$ ($\sin 2\xi$) for the $A2$ ($B2$) terms. We solve eq. (13) using singular value decomposition. The data in eq. (11) have non-zero covariances. Testing shows that ignoring them while solving eq. (13) does not affect the solution.

In the ideal case, 10 events recorded at 10 close stations will result in 50 model parameters with 450 data points. However, we only use delays for station pairs that are no further than 10° apart so that outside-array structure can be largely eliminated as the cause

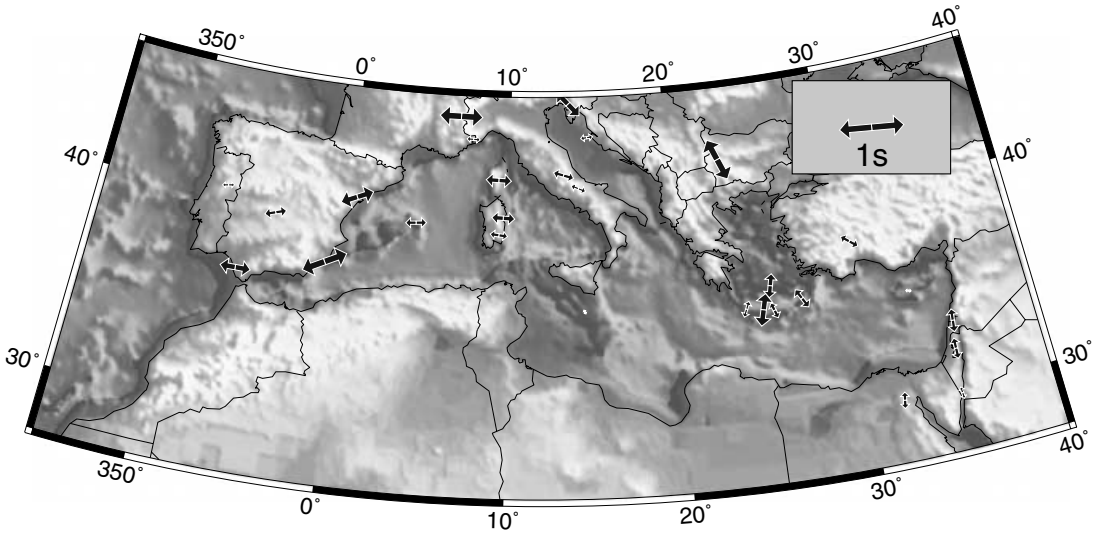

Figure 9. (*Continued.*)

of the delays. Furthermore, delays at stations with an incomplete azimuthal coverage are only expanded to the azimuth independent term $A0$.

3.4 Results

Fig. 9(a) shows the zeroth-order P terms from eq. (13). The root mean square (rms) of the relative delay times in d is 1.1 s. The system of eq. (13) is formally overdetermined and thus has a trivial null space and a unique solution. However, we choose to truncate the Singular Value Decomposition (SVD) because few combinations of variables have such large uncertainties associated with them, for which we prefer the minimum-norm solution. Solving eq. (13), while keeping 95 per cent of the singular values explains 0.4 s of this rms relative delay. Keeping more singular values results in a less than 0.01 s increase of this explained delay. Inverting for the zeroth-order term alone explains 0.3 s of the rms delay time, which is approximately two standard deviations less than when all terms in eq. (13) are included, but does not alter the pattern of positive and negative delays shown in Fig. 9(a). The rms difference between the $A0$ terms of the two inversions is 0.2 s. The difference is largest (up to 0.5 s) for some stations near the edge of the study region. While we expect that an inversion of the relative delay times for 3-D seismic velocity structure will explain significantly more of the observed relative delays, the considerable reduction in rms residual achieved by our inversion for station terms provides an insightful view of main structure in the Mediterranean upper mantle.

The most remarkable early arrivals are seen along the Hellenic arc, while late arrivals occur along the Dead Sea transform. Early arrivals in P are also seen along the Calabrian arc and across the Eurasia–Africa plate boundary in southern Spain and Morocco, therefore current and past subduction zones appear fast. The fact that the Calabrian subduction zone is showing a weaker signal than the Hellenic subduction zone is partly a result of the distribution of event backazimuths, in the latter case the the downgoing lithosphere is better sampled. However, the weaker negative signal may additionally be caused by the smaller amount of material that subducted beneath Calabria (Faccenna *et al.* 2003).

Zeroth-order S terms are shown in Fig. 10. The pattern shown in Fig. 10 is similar to the one seen in Fig. 9(a) in regard to the dominant features.

Because we are interested in the relation between anisotropy and the delay times, we compare the delay times with the splitting times obtained in the previous section. If anisotropy is caused by coherent deformation of the lithosphere, the splitting times should correlate with lithospheric thickness, assuming that the percentage of anisotropy remains constant. Stations located over thin lithosphere should show small splitting times, as opposed to stations over thick lithosphere, where large splitting times are expected. The thickness of the lithosphere should partly be reflected in traveltime delays, as a thick lithosphere will cause early arrivals. Therefore, we may see a negative correlation between delay and splitting times. A positive correlation is expected if anisotropy is caused in the asthenosphere, a thicker asthenosphere implies warmer temperatures and enhanced anisotropy (Savage 1999), but lower seismic velocities. However on Fig. 11, where splitting times are plotted against S delay times, no correlation is apparent. The individual geographical domains likewise do not show that the S delay times correlate with the splitting times there. Therefore, we conclude that azimuthal anisotropy in the Mediterranean region is not confined to the lithopshere or asthenosphere alone. A similar conclusion has been drawn for surface wave polarization anisotropy (Marone *et al.* 2004).

3.4.1 Higher order terms

The higher order terms for P are shown in Figs 9(b) and (c). We did not calculate higher order S terms as a result of the smaller amount of data.

The first-order azimuthal terms for stations located close to subduction zones point in the direction of subduction and therefore most likely map lateral heterogeneity. Anisotropy does not contribute to the first-order term, if the axis of symmetry is horizontal (Schulte-Pelkum *et al.* 2001). Only with a dipping axis of symmetry will there be an effect. However, there is no significant correspondence between the first-order terms and possibly dipping axes inferred from our *SKS* splitting analysis. We conclude that lateral heterogeneity dominates this first-order term.

The second-order azimuthal term would not be zero if the axis of symmetry were horizontal. In fact, the second-order pattern, shown in Fig. 9(c), resembles that obtained from *SKS* splitting, shown in Fig. 6. In Fig. 12, a histogram is shown of the difference between the second azimuthal term and the fast axes of anisotropy. Half of the

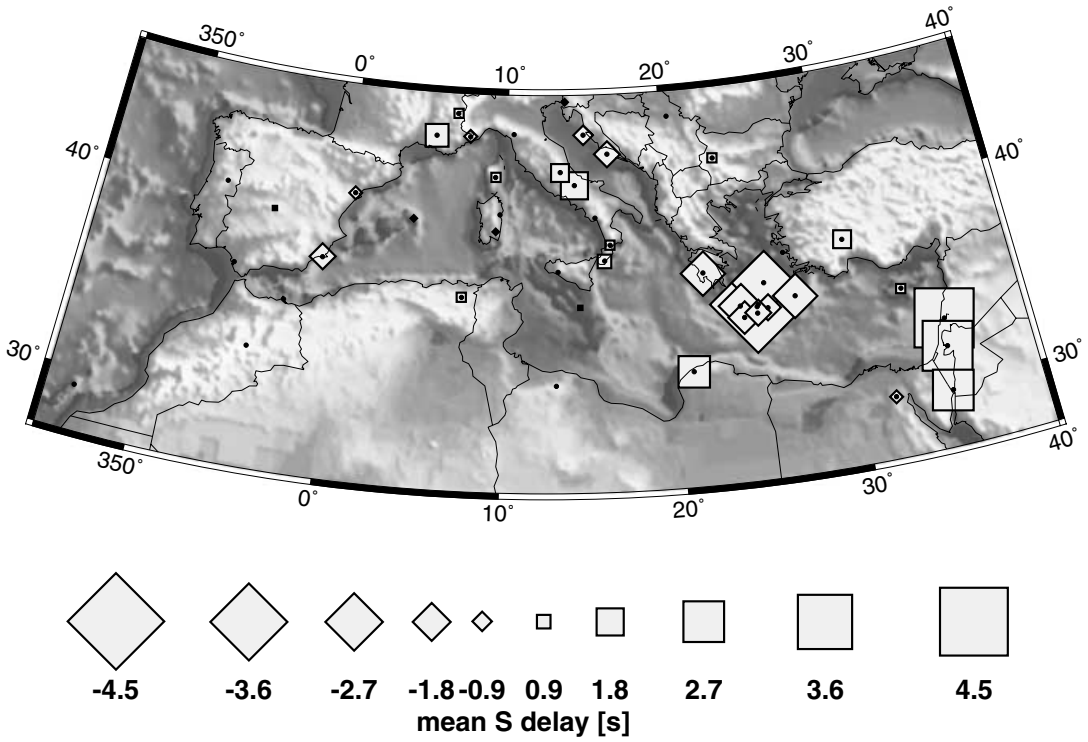

Figure 10. Map of the static *S* term, dominated by large-scale isotropic velocity heterogeneity.

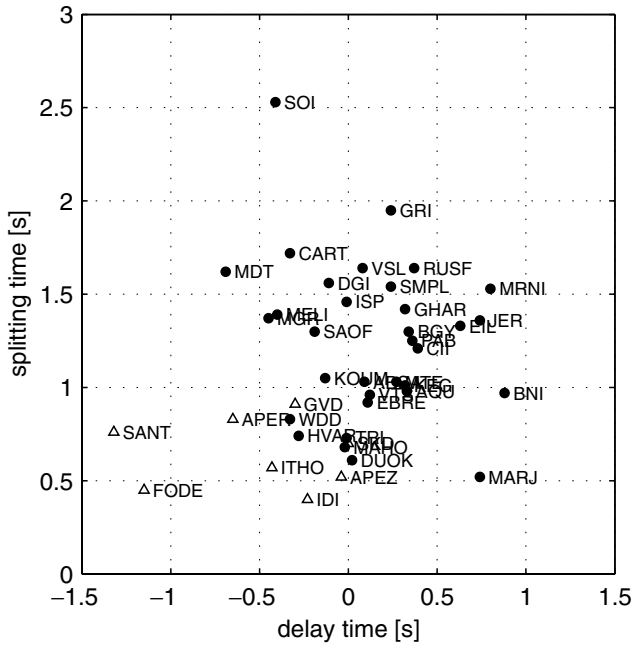

Figure 11. Plot of splitting time versus delay time. Stations along the Hellenic arc are shown with open triangles, other stations with black circles.

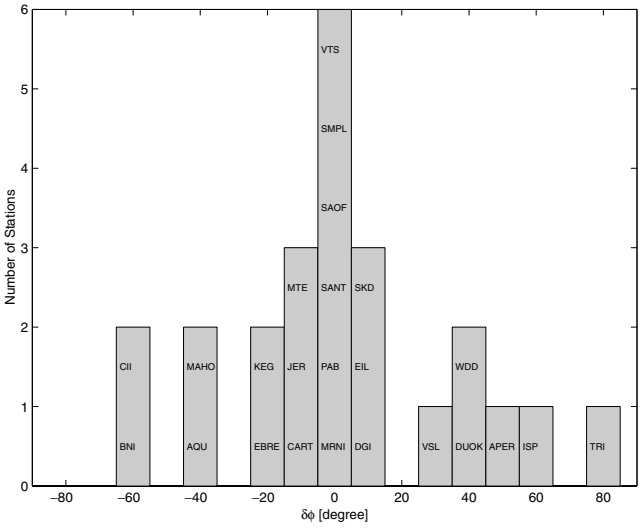

Figure 12. Histogram of difference between the azimuth of the fast axis of anisotropy Φ (Fig. 6) and the azimuth of fast second azimuthal *P* term (Fig. 9).

stations have a difference between the second azimuthal term and the fast axes of anisotropy of less than ± 15°. Given uncertainties of more than 10° in the fast directions of both *SKS* and the second-order delay time terms, this difference implies a good correlation for these stations between the two sets of fast directions. As was the case in Fig. 7, the distribution shown in Fig. 12 is also different from one expected from a uniform distribution, again estimated using a χ^2 test. Such a correlation is not necessarily expected because the teleseismic body waves arrive with small incidence angles and are thus much less sensitive to anisotropy with a horizontal symmetry axis than *SKS* waves. Slightly dipping axes of symmetry would considerably increase the effect on the second-order azimuthal delay time terms (Schulte-Pelkum & Blackman 2003).

We have not calculated azimuth-dependent station terms for *S*. As is evident from the splitting analysis, anisotropy may have a large influence on the delay times. Consider Fig. 13 as an example, where a split *S* arrival is shown for three stations. For these particular event–station combinations, the splitting is so obvious

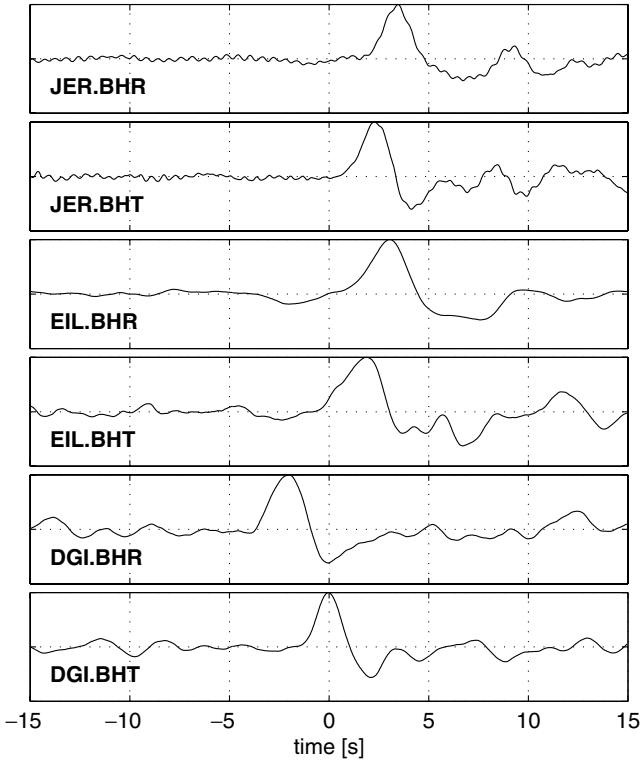

Figure 13. Example of *S* arrival time differences on the horizontal components for the 1999 November 11 (day 315) Northern Sumatera event. The radial and transverse components of three stations are shown, zero time corresponds to the theoretical arrival time. At EIL and JER, the transverse component is earlier than the radial, the opposite is observed at DGI. Backazimuth is 89° for DGI, 102° for EIL and 103° for JER. The backazimuth is perpendicular to the fast axes of anisotropy at EIL and JER, but parallel to the fast axis at DGI (Table 1).

because the backazimuth is either parallel or perpendicular to the fast axis of anisotropy, so that the transverse and radial components show the isolated fast or slow arrival. However, this is an exception and normally the effect of anisotropy is less systematic than in the case of *P*, where the polarization direction is always the same for given backazimuth and distance. The polarization of *S* depends on the radiation pattern. For one backazimuth, we may record only the slow *S* wave, only the fast *S* wave or both, depending on the initial polarization. Therefore anisotropy manifests itself on the delay times in the form of increased scatter on the data. Furthermore, anisotropy tends to distort the waveform, because in general we record a mixture of the slow and fast arrival on the transverse component, with the result that at least we will have a large error in the waveform cross-correlation or that the record may not be used at all. To illustrate what the effect of anisotropy on the station terms may be, we calculated a synthetic set of delay times solely caused by anisotropy. We make the simplified assumption that the initial polarization is perpendicular to the backazimuth and then calculate delay times using,

$$\delta t \approx 0.5 \cdot t_s \cos\left[2(\theta - \phi_s)\right], \tag{14}$$

where T_s and ϕ_s are the splitting parameters and θ is the backazimuth. We then calculated the static *S* terms using the identical event–station distribution for the measurements. The result is shown in Fig. 14, where delays are shown on the same scale as is Fig. 10. In comparison with Fig. 10, most stations only show a small influence of anisotropy.

3.5 *S*/*P* ratio

Seismograms that yielded both *P* and *S* delay times were used for a comparison of the two types of delays. The relation between *P* and *S*

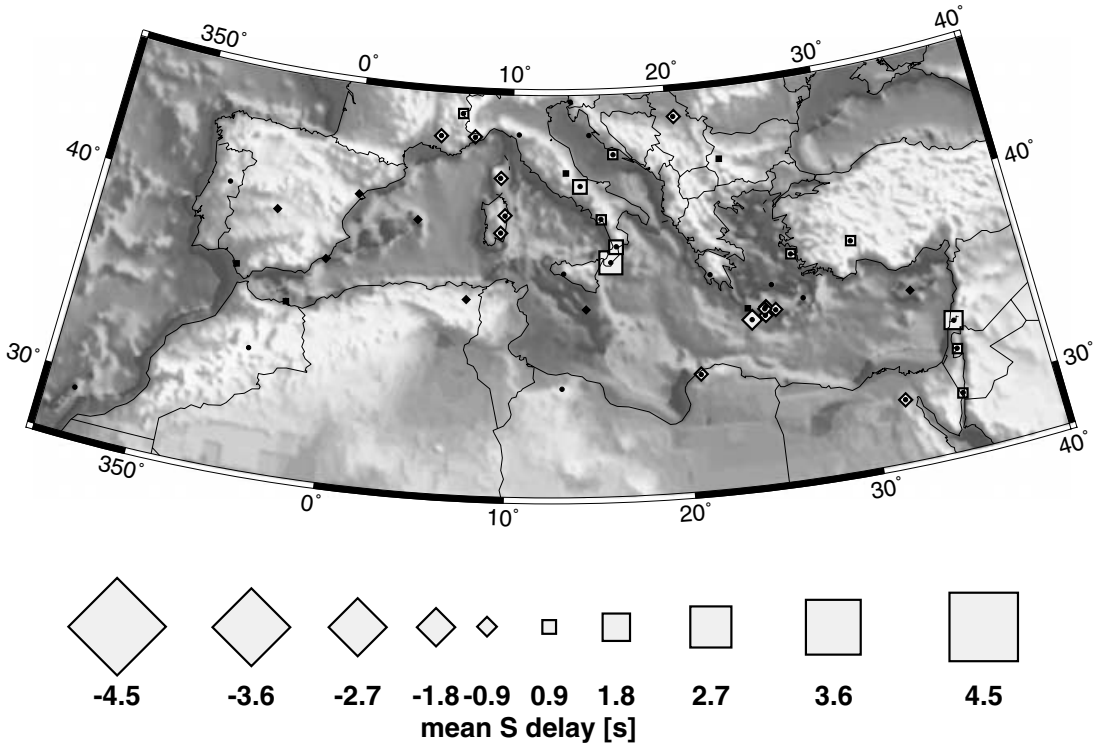

Figure 14. Map of synthetic static *S* term. We calculated synthetic *S* delays caused solely by anisotropy and inverted them in the same way as the data (Fig. 10).

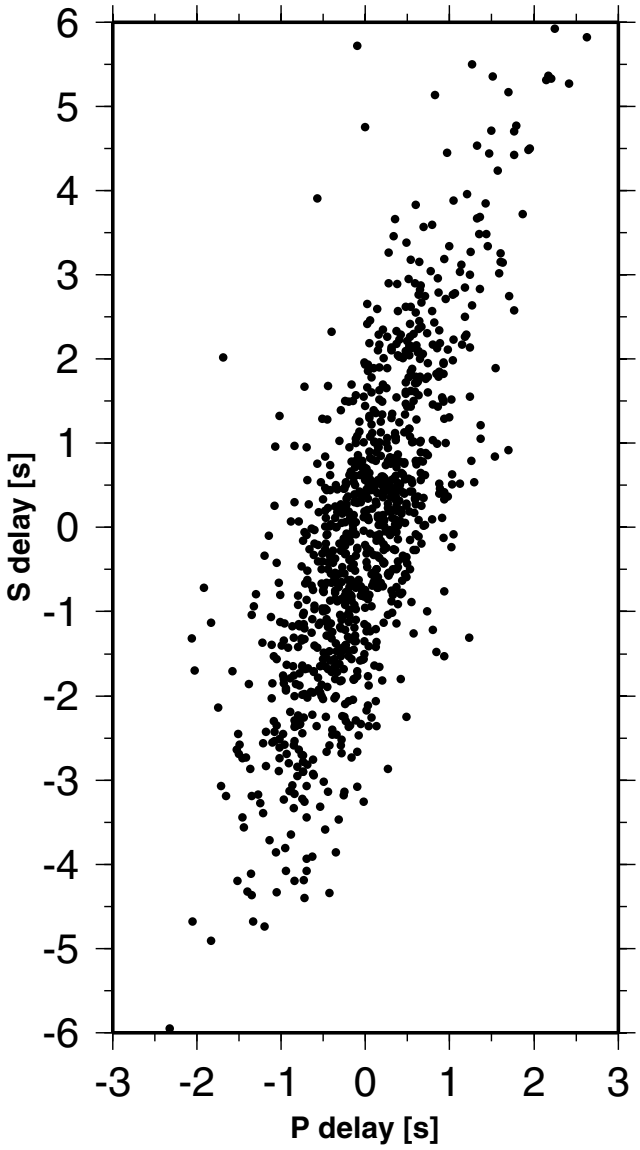

Figure 15. *S* delays versus *P* delays.

delays contains information about the origin of the seismic anomalies, if they are of thermal or chemical in nature. Fig. 15 shows a plot of *S* versus *P* delay. There is a clear correlation between *S* and *P* delays. We estimate the slope of a straight line through these points using the method described in Press *et al.* (1992), which takes into account errors in both the *P* and the *S* delays. The slope is 3.1 ± 0.1, where the uncertainty is estimated using bootstrapping.

This value is in the range of global estimates of this slope by Robertson & Woodhouse (1997) and Bolton & Masters (2001), who report values of 2.85 and 3.2–3.4 respectively. Note that Bolton & Masters (2001) estimate the dependencies of the ratio on the turning depth of the ray and for deeply turning rays they report significantly higher ratios of up to 7.2. This indicates that the relative delays we derived are indeed mostly caused by upper-mantle structure, even though a considerable number of the events used occurred at relatively large distances.

The first-order relation between delay times and variations in seismic velocities is given by

$$\frac{\delta t_\beta}{\delta t_\alpha} \approx \frac{\alpha^2 \delta\beta}{\beta^2 \delta\alpha}, \tag{15}$$

as can be be derived from Fermat's principle.

Of common use in mineral physics studies as well as in joint *P* and *S* seismic tomography is the ratio

$$R_{\beta/\alpha} = \frac{\delta \ln\beta}{\delta \ln\alpha} = \frac{\alpha}{\beta}\frac{\delta\beta}{\delta\alpha} \approx \frac{\beta}{\alpha}\frac{\delta t_\beta}{\delta t_\alpha}. \tag{16}$$

Using the average upper-mantle ratio $\alpha/\beta = 1.81$ of AK135, our estimate of the delay time ratio of 3.1 implies an $R_{\beta/\alpha} \approx 1.7 \pm 0.05$ and $\delta\beta \approx \delta\alpha$. These ratios are consistent with thermal anomalies (Cammarano *et al.* 2003).

However, considerable scatter larger than measurement errors is also evident in Fig. 15. This scatter has several causes. Even for identical sources and receivers, the ray paths for *P* and *S* are not equal and therefore slightly different parts of the mantle are sampled. Scatter is also expected when variations in bulk and shear modulus do not have a constant correlation coefficient, because changes in bulk modulus only affect compressional velocity α. We did not discern regional variations of the S/P ratio in our data.

4 CONCLUSIONS

We have estimated and mapped azimuthal anisotropy throughout the Mediterranean region. Azimuthal anisotropy is widespread in this region. We discern five distinct anisotropic domains:

(i) a western domain in which the pattern of roughly E–W trending fast axes is laterally coherent and aligns with plate motions;

(ii) a northern African domain where, with the exception of two stations (WDD and GHAR), the fast axes align with African Plate motion around a relatively close Euler pole;

(iii) an Apenninic domain where fast axes are parallel to the arcuate mountain belt and thus to the strike of recently (central Italy) and currently (southern Italy) subducting lithosphere;

(iv) an eastern domain where, with the exception of two stations (BGY and ISP), splitting is relatively small and fast axes are laterally incoherent, except along the Dinarides (with fast axes perpendicular to mountain belt) and in the Aegean (with N–S fast axes); and

(v) a far-eastern domain in which N–S fast axes align with Arabian plate motion and relative African–Arabian strike-slip.

While we feel that data coverage needs to be further improved (in particular in northern Africa and eastern Europe) in order to explain the more intricate patterns of anisotropy (in particular the exceptions in the above described domains and the incoherent measurements in the eastern domain) we glean the following overall conclusions. Given the incoherency of surface geologic patterns and styles of deformation in the Mediterranean region, the coherency of fast axes in the western, the northern African and the far-eastern domain has its most likely explanation as the direction of maximal strain in current mantle deformation that is spatially and temporally coherent, such as that related to plate motions. In the western domain, the southeastward extension of the Tyrrhenian sea might also contribute to such strain. In the far-eastern domain, a slight difference between the directions of absolute and relative plate motions suggests that the shallower, more lithospheric mantle could contribute more to the fast axes here, which align better with relative strike-slip plate motion, than to those in the western and northern African domain. The fast axes in the Apenninic domain have their simplest explanation in the ubiquitous subduction below the Italian peninsula, as caused either by corner flow in a hydrated mantle wedge, by trench-parallel flow,

or, at least in part, by shallow lithospheric deformation perpendicular to the direction of compression.

We further measured teleseismic *P* and *S* delay times using a waveform cross-correlation method. We also investigated a dependence of the *P* delays on frequency. For periods from 1 to 20 s, the delay times vary by not more than half a second, which is 20 per cent of the measured relative delay times. Based on the observed slight but probable frequency dependence, we estimate that a significant amount of heterogeneity with scale lengths greater than 200 km exists in the Mediterranean upper mantle. Teleseismic delay times correspond to upper-mantle structure, subduction zones such as the Hellenic Arc appear fast, while late arrivals occur along the Dead Sea transform. We have further determined the azimuthal dependence of teleseismic delay times in order to estimate the influence of anisotropy. We find that lateral heterogeneity is the main contribution to the measured delays and exceeds the influence of anisotropy. However, we do find a correspondence between fast axes estimated from *SKS* splitting and the second azimuthal *P*-wave delay time term, which may be explained by a small dip in the axis of symmetry.

P and *S* delay times are linearly correlated with a coefficient of 3.1. A comparison of this value with that found in global studies indicates that the observed delays are caused largely by seismic heterogeneities in the Mediterranean upper mantle.

ACKNOWLEDGMENTS

The authors are grateful for constructive reviews by Tom Hearn and Martha Savage. In particular, the comments and computations by Tom Hearn improved the statistics used throughout this paper. Funding for this study was provided in part by the Swiss National Science Foundation (SNF 2000-063725). The MIDSEA seismic array was funded by the SNF, with additional support from the Carnegie Institution of Washington, the French National Scientific Research Centre and the University of Nice at Sophia-Antipolis, the Italian National Institute of Geophysics and Volcanology and local organizations (see Van der Lee *et al.* 2001). The authors thank the individuals associated with MIDSEA (see Van der Lee *et al.* 2001). This is contribution number 1358 of the Institute of Geophysics, ETH Zürich.

REFERENCES

Babuška, V., Plomerová, J. & Šilený, J., 1993. Models of seismic anisotropy in the deep continental lithosphere, *Phys. Earth. planet. Int.,* **78,** 167–191.

Bassin, C., Laske, G. & Masters, G., 2000. The Current Limits of Resolution for Surface Wave Tomography in North America, *EOS, Trans. Am. geophys. Un.,* **81,** F897.

Bird, P., 2003. An updated digital model of plate boundaries, *Geochem. Geophys. Geosyst.,* **4,** 1027, doi:10.1029/2001GC000252.

Bolton, H. & Masters, G., 2001. Travel times of *P* and, *S* from the global digital seismic networks: Implications for the relative variation of *P* and *S* velocity in the mantle, *J. geophys. Res.,* **106,** 13 527–13 540.

Boschi, E., Giardini, D. & Morelli, A., 1991. MedNet: the very broad-band seismic network for the Mediterranean, *Il Nuovo Cimento,* **14,** 79–99.

Cammarano, F., Goes, S., Vacher, P. & Giardini, D., 2003. Inferring upper mantle temperatures from seismic velocities, *Phys. Earth planet. Int.,* **138,** 197–222.

Cleary, J. & Hales, A.L., 1966. An analysis of travel times of *P* waves to North American stations in distance range 32 degrees to 100 degrees, *Bull. seism. Soc. Am.,* **56,** 467–489.

Crampin, S., 1981. A review of wave motion in anisotropic and cracked elastic media, *Wave Motion,* **3,** 343–391.

Dercourt, J. *et al.*, 1986. Geological evolution of the Tethys Belt from the Atlantic to the Pamirs since the Lias, *Tectonophysics*, **123,** 241–315.

Dziewonski, A.M. & Anderson, D.L., 1983. Travel times and station corrections for *P* waves at teleseismic distances, *J. geophys. Res.,* **88,** 3295–3314.

Dziewonski, A.M. & Gilbert, F., 1976. The effect of small, aspherical corrections on travel times and a re-examination od the corrections for ellipicity, *Geophys. J. R. astr. Soc.,* **44,** 7–17.

Engdahl, E.R., van der Hilst, R. & Buland, R., 1998. Global teleseismic earthquake relocation with improved travel times and procedures for depth determination, *Bull. seism. Soc. Am.,* **88,** 722–743.

Faccenna, C., Jolivet, L., Piromallo, C. & Morelli, A., 2003. Subduction and the depth of convection in the Mediterranean mantle, *J. geophys. Res.,* **108,** 2099, doi:10.1029/2001JB001690.

Gledhill, K. & Gubbins, D., 1996. *SKS* splitting and the seismic anisotropy of the mantle beneath the Hikurangi subduction zone, New Zealand, *Phys. Earth. planet. Int.,* **95,** 227–236.

Gvirtzman, Z. & Nur, A., 1999. The formation of Mount Etna as the consequence of slab rollback, *Nature,* **401,** 563–566.

Hanka, W. & Kind, R., 1994. The GEOFON program, *IRIS Newsletter*, **13,** 1–4.

Hatzfeld, D. *et al.*, 2001. Shear wave anisotropy in the upper mantle beneath the Aegean related to internal deformation, *J. geophys. Res.,* **106,** 30 737–30 754.

Hearn, T.M., 1999. Uppermost mantle velocities and anisotropy beneath Europe, *J. geophys. Res.,* **104,** 15 123–15 139.

Hess, H.H., 1964. Seismic anisotropy of the uppermost mantle under oceans, *Nature*, **203,** 629–631.

Jung, H. & Karato, S., 2001. Water-induced fabric transitions in olivine, *Science*, **293,** 1460–1463.

Kaminski, É. & Ribe, N.M., 2002. Timescales for the evolution of seismic anisotropy in mantle flow, *Geochem. Geophys. Geosyst.,* **3,** 1051, doi:10.1029/2001GC000222.

Kennett, B.L.N., Engdahl, E.R. & Buland, R., 1995. Constraints on seismic velocities in the Earth from travel-times, *Geophys. J. Int.,* **122,** 108–124.

Laske, G., 1995. Global observation of off-great circle propagation of long-period surface waves, *Geophys. J. Int.,* **123,** 245–259.

Mainprice, D. & Silver, P.G., 1993. Interpretation of *SKS*-waves using samples from the subcontinental lithosphere, *Phys. Earth. planet. Int.,* **78,** 257–280.

Mardia, K.V. & Jupp, P.E., 2000. *Directional Statistics*, John Wiley & Sons, Chichester, UK.

Margheriti, L., Lucente, F.P. & Pondrelli, S., 2003. *SKS* splitting measurments in the Apenninic-Tyrrhenian domain (Italy) and their relation with lithospheric subduction and mantle convection, *J. geophys. Res.,* **108,** 2218, doi:10.1029/2002JB001793.

Marone, F., van der Meijde, M., van der Lee, S. & Giardini, D., 2003. Joint inversion of local, regional and teleseismic data for crustal thickness in the Eurasia-Africa plate boundary region, *Geophys. J. Int.,* **154,** 499–514.

Marone, F., van der Lee, S. & Giardini, D., 2004. Shallow anisotropy in the Mediterranean mantle from surface waves, *Geophys. Res. Lett.,* **31,** L06624, doi:10.1029/2003GL018948.

Marson-Pidgeon, K. & Savage, M.K., 1997. Frequency-dependent anisotropy in Wellington, New Zealand, *Geophys. Res. Lett.*, **24,** 3297–3300.

McKenzie, D.P., 1970. Plate Tectonics of the Mediterranean region, *Nature,* **226,** 239–243.

Meijer, P.T. & Wortel, M.J.R., 1997. Present-day dynamics of the Aegean region: A model analysis of the horizontal pattern of stress and deformation, *Tectonics*, **16,** 879–895.

Müller, G., Roth, M. & Korn, M., 1992. Seismic -wave traveltimes in random media, *Geophys. J. Int.,* **110,** 29–41.

Müller, R.D., Royer, J.-Y. & Lawver, L.A., 1993. Revised plate motions relative to the hotspots from combined Atlantic and Indian Ocean hotspot tracks, *Geology,* **21,** 275–278.

Piromallo, C. & Morelli, A., 2003. *P* wave tomography of the mantle under the Alpine-Mediterranean area, *J. geophys. Res.,* **108,** 2065, doi:10.1029/2002JB001757.

Press, W.H., Teukolsky, S.A., Veterling, W.T. & Flannery, B.P., 1992. *Numerical Recipes in Fortran: The Art of Scientific Computing*, 2nd edn, Cambridge University Press, Cambridge, UK.

Rümpker, G. & Silver, P.G., 1998. Apparent shear-wave splitting parameters in the presence of vertically varying anisotropy, *Geophys. J. Int.,* **135,** 790–800.

Rümpker, G., Tommasi, A. & Kendall, J.-M., 1999. Numerical simulations of depth-dependent anisotropy and frequency-dependent wave propagation effects, *J. geophys. Res.,* **104,** 23 141–23 154.

Robertson, G.S. & Woodhouse, J.H., 1997. Comparison of *P* and, *S* station corrections and their relationship to upper mantle structure, *J. geophys. Res.,* **102,** 27 355–27 366.

Russo, R.M. & Silver, P.G., 1994. Trench-parallel flow beneath the Nazca plate from seismic anisotropy, *Science,* **263,** 1105–111.

Saltzer, R.L., Gaherty, J.B. & Jordan, T.H., 2000. How are vertical shear wave splitting measurements affected by variations in the orientation of azimuthal anisotropy with depth?, *Geophys. J. Int.,* **141,** 374–390.

Savage, M.K., 1999. Seismic anisotropy and mantle deformation: What have we learned from shear wave splitting?, *Rev. Geophys.,* **37,** 65–106.

Schulte-Pelkum, V. & Blackman, D.K., 2003. A synthesis of seismic *P* and, *S* anisotropy, *Geophys J. Int.,* **154,** 166–178.

Schulte-Pelkum, V., Masters, G. & Shearer, P.M., 2001. Upper mantle anisotropy from long-period *P* polarization, *J. geophys. Res.,* **106,** 21 917–21 934.

Sella, G.F., Dixon, T.H. & Mao, A., 2002. REVEL: a model for recent plate velocities from space geodesy, *J. geophys. Res.,* **107,** 2099, doi:10.1029/2000JB000033.

Silver, P.G., 1996. Seismic anisotropy beneath the continents: probing the depths of geology, *Ann. Rev. Earth planet. Sci.,* **24,** 385–432.

Silver, P.G. & Chan, W.W., 1991. Shear wave splitting and subcontinental mantle deformation, *J. geophys. Res.,* **96,** 16 429–16 454.

Silver, P.G. & Savage, M.K., 1994. The interpretation of shear-wave splitting parameters in the presence of 2 anisotropic layers, *Geophys. J. Int.,* **119,** 949–963.

Tong, J., Dahlen, F.A., Nolet, G. & Marquering, H., 1998. Diffraction effects upon finite-frequency travel times: a simple 2-D example, *Geophys. Res. Lett.*, **25,** 1983–1986.

Van der Lee, S. *et al.,* 2001. Eurasia-Africa plate boundary region yields new seismographic data, *EOS, Trans. Am. geophys. Un.,* **82**(51), 637–646.

VanDecar, J.C. & Crosson, R.S., 1990. Determination of teleseismic relative phase arrival times using multi-channel cross-correlation and least-squares, *Bull. seism. Soc. Am.,* **80,** 150–169.

Vinnik, L.P. & Kind, R., 1993. Ellipticity of teleseismic *S*-particle motion, *Geophys. J. Int.,* **113,** 165–174.

Wortel, M.J.R. & Spakman, W., 2000. Subduction and slab detachment in the Mediterranean-Carpathian region, *Science,* **290,** 1910–1917.